

Low loss hybrid Nb/Au superconducting resonators for quantum circuit applications

M. C. de Ory¹, D. Rodriguez¹, M. T. Magaz¹, V. Rollano^{2,3,*}, D. Granados⁴, and A. Gomez^{1,*}

¹Centro de Astrobiología (CSIC - INTA), Torrejón de Ardoz, 28850 Madrid, Spain.

²Instituto de Nanociencia y Materiales de Aragón (CSIC - UNIZAR), 50009, Zaragoza, Spain.

³Shanghai Branch, CAS Center for Excellence in Quantum Information and Quantum Physics, University of Science and Technology of China, Shanghai 201315, China

⁴IMDEA Nanociencia, Cantoblanco, Madrid 28049, Spain

January 29, 2024

Abstract

Superconducting resonators play a crucial role in developing forthcoming quantum computing schemes. The complete integration of molecular spin-based quantum bits with superconducting resonators still requires further developments, notably in maintaining low-loss resonances and high quality factors. In this work, we have developed a superconducting device combining a niobium (Nb) circuit with a 10 nm gold (Au) capping layer, which supports low microwave losses and enables new functionalities such as the integration of magnetic molecules into solid-state devices. Our investigation across a wide temperature and driving power range reveals that adding the Au layer reduces the density of two-level system (TLS) defects present in the device. Moreover, the presence of the thin Au layer induces a higher kinetic inductance at low temperatures, leading to enhanced responsivity. Cryogenic characterization confirms the good performance of the device, allowing these resonators to serve as platforms for hybrid devices involving molecular spin qubits/gates where the gold can anchor alkyl thiol groups to form self-assembled monolayers. Our findings suggest the potential of Nb/Au lumped element resonators (LERs) as versatile and promising tools for advancing superconducting quantum technologies and the integration of quantum functionalities into solid-state devices.

Introduction

Superconducting microwave resonators are key building blocks in the development of different technologies with a wide range of applications including quantum computing [1], quantum communication [2], quantum sensing [3, 4] or cavities for particle accelerators [5]. These superconducting resonators stand out for their high internal quality factor (Q_i) which essentially quantifies its electromagnetic (EM) energy loss rate; a higher Q_i implies longer EM energy storage, enabling higher integration times and, thus, higher signal to noise ratio (SNR). Typically, the value of Q_i is limited by different dissipative sources including radiation losses, superconducting vortices or residual surface resistance; among others [6, 7]. In the single photon and low-temperature limits, Q_i is predominantly limited by the parasitic noise generated by two-level systems (TLSs) developed via trapped charges and electric dipoles naturally present in amorphous dielectric layers in contact with the superconductor, such as native oxides at its surface or the substrate/superconductor interface. TLSs couple to the resonator electric field [8, 9], inducing non-desired energy dissipation and decoherence, lowering, and thus degrading the device performance. Therefore, reducing or even eliminating TLSs is a must to attain better control of the microwave losses and boost the resonator performance.

In this sense, ongoing research continues into developing resonators with reduced TLS noise [10]. Different strategies have been approached, including the optimization of the nanofabri-

cation processes [11], substrate choice [12], surface treatment [13], resonator design [14, 15], or the use of different superconducting materials [12, 16, 17]. Typical superconducting materials employed for developing high-quality resonators include niobium (Nb) or aluminum (Al), depending on the application. For instance, Al is widely used to develop Kinetic Inductance Detectors, state-of-the-art radiation detectors typically used for astrophysics experiments [18]. On the other hand, Nb resonators are preferred for quantum computing applications, as their higher critical temperature ($T_c \sim 9$ K) and larger critical field lead to better stability against temperature and magnetic field fluctuations. Furthermore, this resilience makes them suitable for quantum applications requiring magnetic fields, opening the path for the implementation of new hybrid quantum architectures based on molecular spins qubits [19, 20] or magnonic excitations [21, 22]. Even though these materials have proven to have very high performance, their internal quality factor is still limited by the noise generated by the TLSs present in the native oxide layer, among others [23].

In this work, we propose using bilayer niobium/gold (Nb/Au) Lumped Element Resonators (LERs). The thin gold layer deposited on top of the niobium film prevents oxidation, enhancing surface stability and reducing the density of TLSs. Thus, the presence of the Au layer contributes to increase the internal quality factor and performance reliability of the resonators. Beyond its role in preserving oxidation of the Nb surfaces, the Au layer also offers advantages in quantum computing and sensing technologies since it increases the kinetic inductance (L_k)

* Corresponding authors: vrollano@unizar.es, agomez@cab.inta-csic.es

of the device while facilitates the integration with molecular systems. Using the Au thickness as a design criterion, the capping layer enables controlling L_k through proximity effect [24, 25]. This parameter relates to the inertia of the superconducting charge carriers when an alternating current is applied and, distinct from its geometric counterpart, it exhibits a strong dependence on current and temperature. This characteristic leads to enhanced responsivity in detectors [26], allows for the tunability of resonance frequency²⁷ and is suitable for development parametric amplifiers [28]. The kinetic inductance contribution increases the characteristic impedance and, therefore, the zero-point voltage fluctuations, making it an ideal platform for efficiently coupling microwave photons to small electric dipole moments [29]. Integration with molecular systems also remains a challenge since the presence of a gap between the resonator and the molecular ensemble crystal wastes the region of the resonator mode volume where the electromagnetic fields are more intense. Self-assembled monolayers (SAMs) of single-molecule spin ensembles can be anchored to the Au surface via thiol groups [30, 31], reducing the gap to zero. This characteristic is desirable for the development of hybrid quantum systems based on molecular-based qubits [20], as it enables the device

to harness the highest magnetic field intensity close to the resonator surface, thereby maximizing the coupling strength with the molecules. Finally, the native oxide of the superconductor surface is a significant obstacle when applying these devices to applications involving scanning tunnelling microscopy (STM) [32]. In this bilayer design, the Au layer improves the performance of the device in STM conditions, avoiding the native oxide, which, together with the possibility of SAMs deposition, opens the door to coherent control of spin qubits on surfaces using Nb superconducting resonators [33, 34]. Moreover, recent studies have shown that using the Nb/Au proximitized film could help increase the spin-based qubits' lifetime [35]. Here, the experimental demonstration of Nb/Au superconducting LERs and its comparison with bare Nb ones is presented. Microwave cryogenic characterization shows a consistent development that matches with designs. We present the dependence of the resonance frequency (f_r) and internal quality factor as a function of driving power and temperature, demonstrating Q_i values up to 0.5M at low power conditions and even greater than 1M at saturation of the TLSs for both systems. Using a dielectric loss model, we find a reduced TLS density when adding the Au as a protective layer.

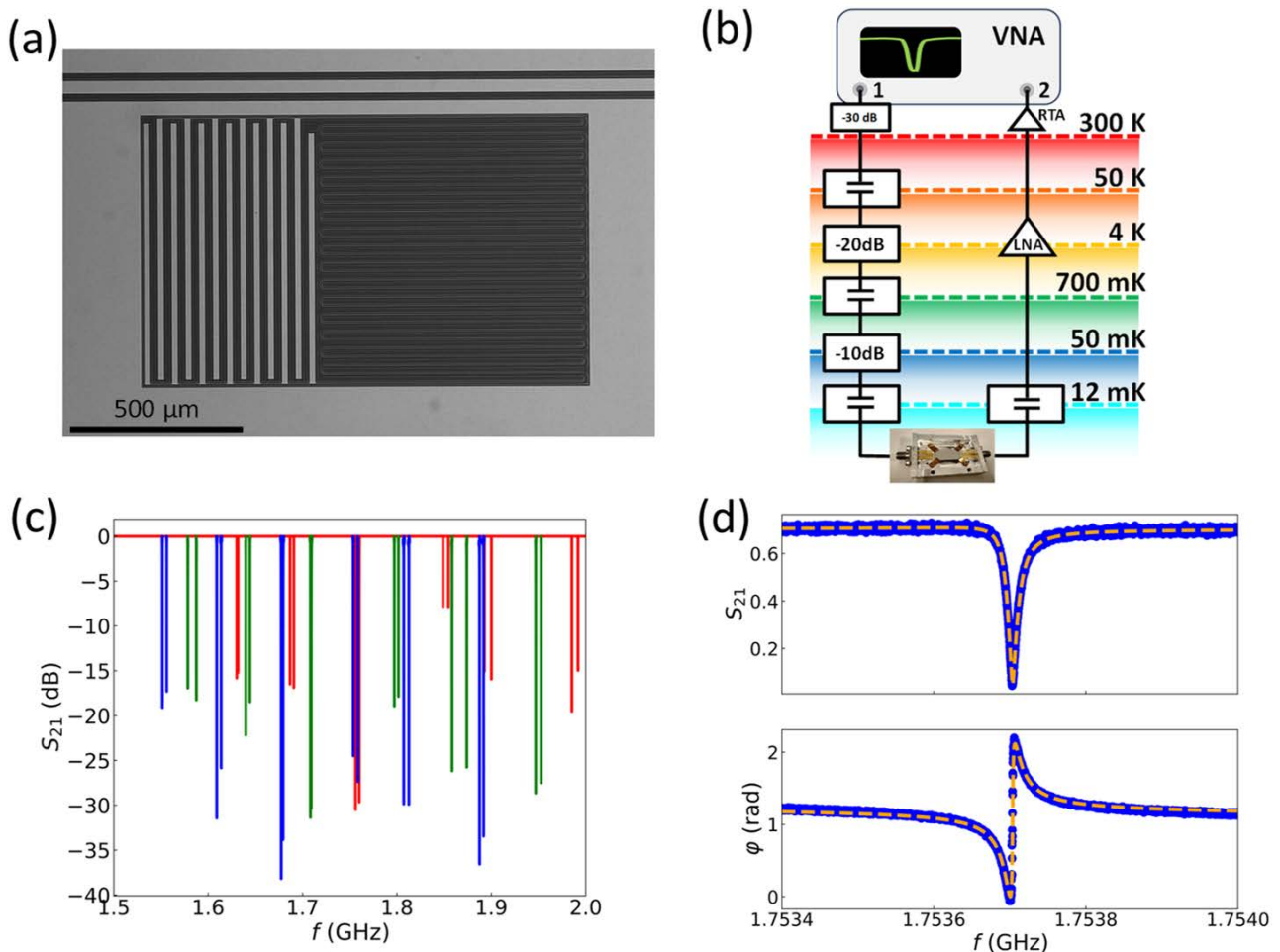


FIG 1. (a) Optical image of one of the fabricated Nb/Au LER. (b) Scheme of the measurement set-up in the $^3\text{He}/^4\text{He}$ dilution refrigerator. High-frequency input coaxial lines are attenuated 30 dB outside the cryostat. The output signal is amplified 35 dB through a Low Noise Amplifier. (c) Amplitude of the transmission as a function of frequency measured for the two chips. Measurements for Nb/Au device is shown in blue while for Nb device is shown in green. Red color depicts the resonances simulated considering $L_k = 0$ pH/sq. (d) Amplitude (up) and phase (down) of the transmission as a function of frequency obtained for a Nb/Au resonator at 15 mK with a driving power of -96 dBm. Blue dots show the experimental data while orange dashed lines show the fit obtained using Equation (1). Parameter values resulting from the fit are $f_r = 1.7537$ GHz, $Q_i = 1.48 \cdot 10^6$ and $Q_c = 7.90 \cdot 10^4$.

Experimental Details

A Nb/Au chip has been manufactured together with a nominally identical control sample fabricated of bare Nb. Each chip includes twelve lumped element inductor-capacitor (LC) resonators coupled in parallel to a single coplanar waveguide transmission line (CPW), which serves for readout. The CPW line is matched to a $50\ \Omega$ impedance, with a center conductor of $40\ \mu\text{m}$ width separated $20\ \mu\text{m}$ from the ground planes. The LERs parameters have been modeled through electromagnetic simulations using Sonnet Suite software [36] where the resonance frequency of each LER is fixed by the geometry of both capacitor and inductor ($f_r = 1/\sqrt{LC}$), whereas the coupling quality factor (Q_c) is set by the distances between the LER and the CPW and ground planes.

The device fabrication process starts with the surface preparation of a $270\ \mu\text{m}$ high-resistivity silicon (Si) substrate ($R > 1\ \text{k}\Omega \cdot \text{cm}$) to remove the native silicon oxide a 1% hydrofluoric acid bath. Immediately afterwards, the sample is introduced in an electron-beam evaporator where the three layers of superconducting film, titanium 2.5 nm / niobium 100 nm / gold 10 nm, are evaporated (the Ti seed layer is used to improve the adhesion to Si). In the case of the bare Nb resonators, Ti 2.5 nm / Nb 100 nm are evaporated in an independent procedure. The patterning process is based on maskless laser-writer photolithography using AZnLOF 2070 negative photoresist. Afterwards, the etching process is performed in three steps: first, the gold film is etched by argon ion milling, then the niobium film is removed using a SF₆:Ar plasma etching and, finally, the Ti is removed using wet etching. The remaining resist is removed in acetone and isopropanol rinse and RF oxygen plasma cleaner. Figure 1a shows an optical image of a fabricated Nb/Au LER as an example.

The devices are cooled down to millikelvin temperatures using a dilution refrigerator (Bluefors LD250). The electrodynamic response is measured with a commercial Vector Network Analyzer (VNA) using the cryogenic harness shown in Figure 1b. The input power is varied from $-80\ \text{dBm}$ to $+5\ \text{dBm}$ from the VNA and attenuated by 30 dB at room temperature, 20 dB in the 4 K stage and 10 dB through the 500 mK stage. DC blocks prevent DC current leakages and provide thermal breaks between stages. The output signal is then amplified by a low-noise amplifier at the 4 K stage and a second amplification stage outside the refrigerator. Stainless steel (SS), CuNi and (superconducting) NbTi cables are used between stages in order to guarantee good electrical conductivity and poor thermal conductivity, whilst copper cables are used to thermalize within the stage. The final devices are mounted in a cold finger in the mixing chamber plate on a superconducting aluminum holder with a PCB, using low temperature varnish (SCBltv01) for thermalization and aluminum wire-bonding for electrical connections. The sample is further magnetically screened using a mu-metal shield (at room temperature). In Figure 1c, we show the S_{21} transmission parameter obtained for the twelve Nb/Au and Nb LERs in each chip measured at 15 mK and applying a driving power of $-96\ \text{dBm}$. The simulated transmission as a perfect conductor (with $L_k = 0\ \text{pH/sq}$) is also plotted for comparison. Each resonance corresponds to a dip in the transmission spectrum (S_{21}). Figure 1d shows the complex transmission spectrum (in amplitude and phase) at 15 mK driven by an input signal of $-96\ \text{dBm}$ for one of the twelve resonances obtained in the Nb/Au chip. The transmission parameter of a resonator can be modeled according to:

$$S_{21} = a \left[1 - \frac{\frac{Q_l}{Q_c}}{1 + 2iQ_l \left(\frac{f-f_r}{f_r} \right)} \right] \quad (1)$$

Where the loaded quality factor (Q_l) is $Q_l^{-1} = Q_i^{-1} + Q_c^{-1}$. We fit the resonance data using the method detailed in [37], obtaining the resonator parameters f_r , Q_i , and Q_c . The fit is shown in Figure 1d in dashed lines.

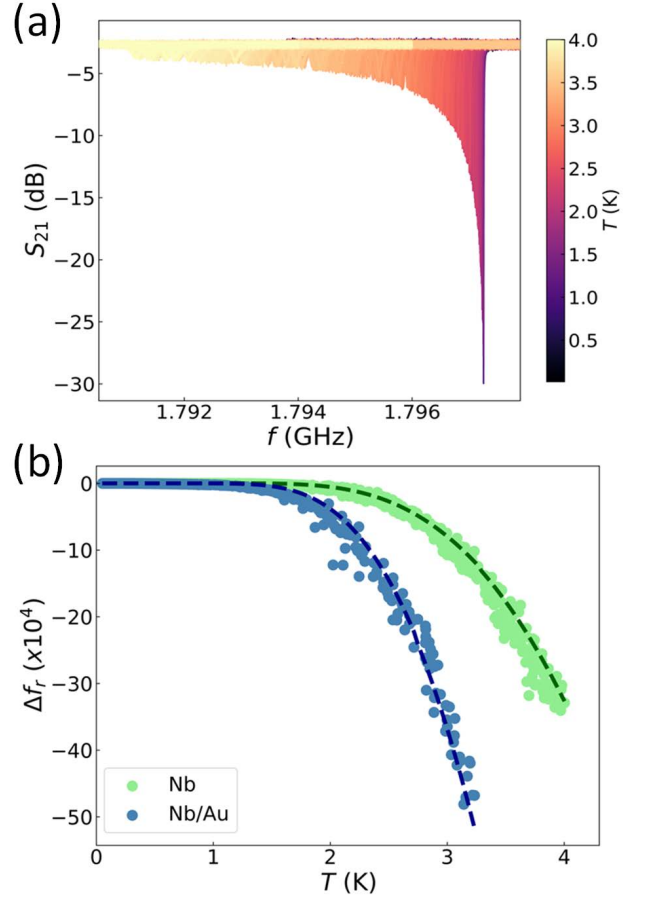


Figure 2. (a) Amplitude of the transmission spectrum in dB as a function of temperature for one Nb resonator measured with a driving amplitude of $-92\ \text{dBm}$. Color scale indicates the chip temperature. (b) Fractional change of the resonance frequency as a function of the chip temperature for a Nb/Au resonator (light blue) and a Nb resonator (light green). Dashed lines depict the Mattis-Bardeen fit upon the experimental data. Nb/Au fit is shown in dark blue while Nb fit is shown in dark green.

Kinetic Inductance Characterization

In Figure 1c the comparison of the transmission spectra for Nb/Au, Nb and simulated designs with $L_k = 0\ \text{pH/sq}$ shows a systematic drop to lower frequencies for Nb/Au compared to the Nb ones. This drop is even more noticeable when comparing with the simulated designs and it is a consistent trend across all twelve resonators. This behavior is attributed to a reduction of the critical temperature in the bilayer material due to proximity effect, which also increases the kinetic inductance ($L_k \approx \hbar R_s \pi^{-1} \Delta_0^{-1}$, with $\Delta_0 = 1.74 k_B T_c$ being the superconducting gap and R_s the sheet resistance). From the experimental results, we have calculated L_k for both materials by comparing the measured resonance frequencies (f_{meas}) with the simulated ones, according to this expression:

$$L_k = \left[\left(\frac{f_{sim}}{f_{meas}} \right)^2 - 1 \right] L_g \quad (2)$$

Where f_{sim} is the resonance frequency of the simulated resonator (with $L_k = 0$ pH/sq) and L_g is the geometric inductance defined by the resonator design. From Equation (2), we obtain a mean value of $L_k = 0.1$ pH/sq for the Nb resonators and $L_k = 0.24$ pH/sq for the Nb/Au ones. Then, the kinetic fraction (α_k), given by L_k over the total inductance ($L_g + L_k$) can be obtained, resulting in mean values of $\alpha_k = 0.055$ for Nb and $\alpha_k = 0.101$ for Nb/Au. The parameter α_k is crucial in developing kinetic inductance detectors, since the higher its value the higher the device responsivity and the lower the noise equivalent power (NEP) can be obtained [38]. Moreover, a higher the α_k also leads to a higher frequency tunability and amplification in superconducting devices developed for quantum applications^{27,28}.

We have performed a temperature sweep in both devices to characterize the resonators response to thermal excitations of the Cooper pair condensate and hence investigate the kinetic inductance of both materials. Figure 2a presents the amplitude of the transmission spectrum as a function of the chip temperature measured for a Nb LER. These measurements have been performed with a low driving power (-92 dBm), where the TLSs are not expected to be saturated. As temperature rises, the peak broadening and the shift to lower resonance frequencies are evident. This is due to the gradual worsening of the superconducting properties in the material. In Figure 2b we show the fractional change in resonance frequency as a function of temperature over a range from 15 mK to 4 K, which is given by $\Delta f_r(T) = (f_r(T) - f_{r,0})/f_{r,0}$, where $f_{r,0}$ is the resonance frequency at the lowest measured temperature (15 mK), at which the superconducting properties of the device are fully recovered.

The ideal response of a superconductor is described by the Mattis-Bardeen (MB) model with a complex conductivity $\sigma_s = \sigma_1 - i\sigma_2$, where the real part describes the dissipative processes or absorption and the imaginary part accounts for the inductive response of the superconductor. The fractional change of the resonance frequency Δf_r is related to α_k and the fractional change of σ_2 by:

$$\Delta f_r(T) = \frac{\alpha_k}{2} \Delta \sigma_2(T) \quad (3)$$

The fits obtained from MB model upon the experimental data shown in Figure 2b are plotted in dashed lines. The data fits using Equation (3) are performed assuming a superconducting gap depending on temperature [39]. The observed downshift in resonance frequency as temperature increases agrees with MB model [40], which predicts a drop in resonance frequency above $T \sim T_c/8$. The obtained values from the fit for this particular LER design are $\alpha_k(Nb) = 0.09$ with $T_c(Nb) = 8.8$ K, whereas $\alpha_k(Nb/Au) = 0.16$ with $T_c(Nb/Au) = 7.3$ K.

TLS influence in the electrodynamic response

The interaction of the devices with the TLSs is mediated through the electric field created by the photons in the resonator. Coupling to TLSs deviates the response of the superconductor from the MB model behavior and, therefore, it can be employed to reveal the TLSs contribution to the resonator

losses. In the low-power regime, when a photon enters the resonator, there is a certain probability for the photon to be absorbed by a TLS instead of being returned back to the transmission line. Then, the TLS relaxes by emitting a phonon into the bath, thus contributing to the loss mechanism and precluding the resonator performance. This is called resonant TLS, only affecting frequencies in a narrow band near resonance frequency ($f_{TLS} \sim f_r$), modifying the resonator parameters (f_r and Q_i). Furthermore, the distribution of TLSs interacting with the resonator is much broader than the resonator bandwidth. This non-resonant TLS changes the charge distribution in the material causing fluctuations in the imaginary part of the dielectric constant, affecting only the f_r thermal dependence [17].

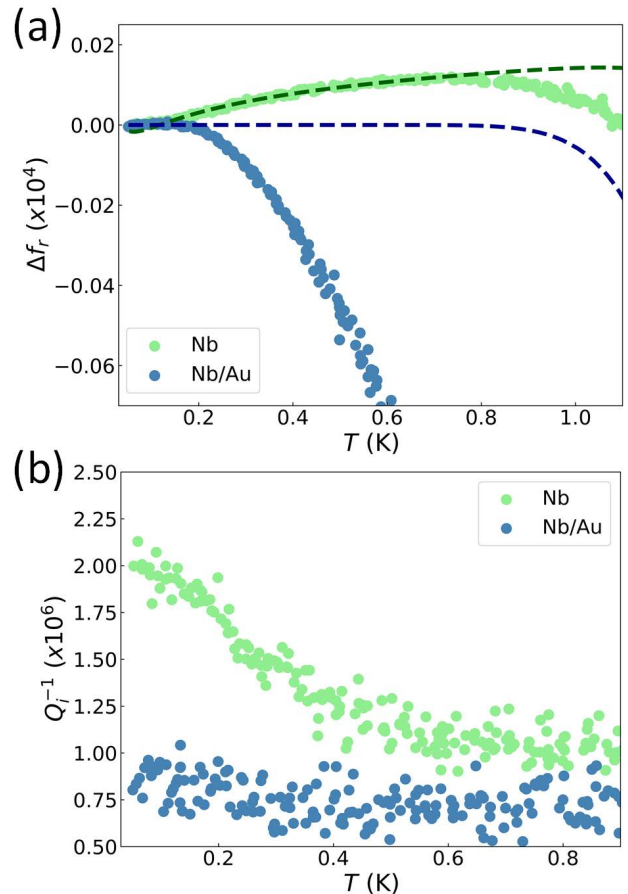


Figure 3. (a) Fractional change of the resonance frequency as a function of the chip temperature in the low-temperature regime. Applied driving power is -92 dBm. Dark green dashed line shows the MB model modified with the TLS contribution for Nb. Dark blue dashed line shows the non-modified MB model for Nb/Au. (b) Inverse of the quality factor as a function of temperature in the low temperature regime for Nb and Nb/Au.

To investigate the contribution of the TLSs to the loss mechanisms in both devices, we have performed a detailed analysis in the low-temperature regime when the TLSs are not thermally saturated and the quasiparticle density is negligible. It is worth noting that these measurements are performed in the low power regime (-92 dBm) where the TLS noise are not power saturated [41, 42]. As can be seen in Figure 3a, in the low temperature limit (between 15 mK and 700 mK) the behavior of the resonance frequency with temperature differs between the two materials. For the Nb device, Δf_r temperature dependence deviates from the MB model, exhibiting an upshift as temperature rises and TLSs saturate. We have modeled this trend originated

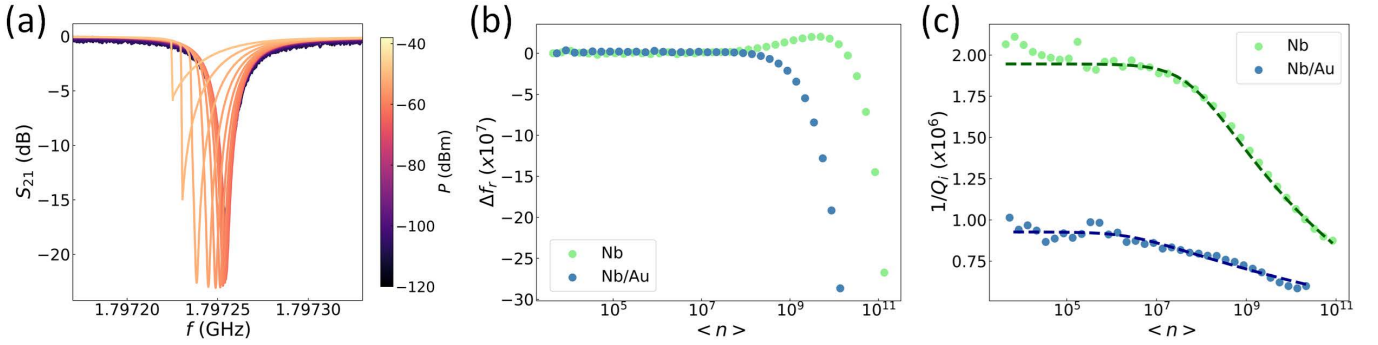


Figure 4. (a) Transmission spectrum as a function of driving power for a Nb LER measured at 15 mK. (b) Fractional resonance frequency shift as a function of photon number for the Nb device (light green) and the Nb/Au one (light blue). The photon number is obtained from Equation (6). (c) Inverse of the internal quality factor ($\tan \delta$) as a function of the number of photons in the resonator. Experimental data in light green circles for Nb and light blue for Nb/Au. Dashed lines (dark green for Nb and dark blue for Nb/Au) show the fit performed using Equation (7) upon the experimental data.

in the interaction with TLSs by adding their contribution to the MB model as $\Delta f_r = \Delta f_r^{MB} + \Delta f_r^{TLS}$, where the change in resonance frequency due to TLSs is given by:

$$\Delta f_r(T) = \frac{F}{2} \Delta \varepsilon(T) + f_{offset} \quad (4)$$

In this expression, F accounts for the fraction of dielectric material filling the resonator volume, and $\Delta \varepsilon$ the fractional change of the dielectric constant over temperature due to TLSs thermal excitation [9], and it is given by:

$$\Delta \varepsilon = \frac{-2\delta}{\pi} \left\{ R \left[\Psi \left(\frac{1}{2} + i \frac{hf}{2\pi k_B T} \right) \right] - \log \left(\frac{hf_r}{k_B T} \right) \right\} \quad (5)$$

The product $\delta \cdot F$ is related to the density of TLSs and the dissipation of the material related to them, and Ψ is the digamma function. Taking this product as a free parameter, dark green dashed line in Figure 3a shows the fit upon the experimental data using this MB modified model, from which we obtain a value of $\delta \cdot F = 5.3 \cdot 10^{-6}$. On the other hand, the Nb/Au device develops a quick drop of the resonance frequency that deviates from the MB theory prediction (shown with a dashed blue line). This may be due to the proximity effect induced by the Au layer in the Nb [43, 44], avoiding a quantitative analysis of the TLSs contribution.

To investigate the nature of the loss mechanism in the devices, we have characterized the internal quality factor thermal dependence in the low temperature regime. In Figure 3b we show the inverse of the internal quality factor as a function of temperature. For the Nb sample, we observe an increase in the internal quality factor, consequence of the thermal saturation of the TLSs for $T_{\text{bath}} = hf/2k_B$. This is in agreement with Equations (4) and (5) and the frequency upshift previously shown in Figure 3a. In contrast, this behavior is not clearly visible for the Nb/Au device, revealing that microwave loss is not predominantly TLS limited and evidencing that the premature deviation from MB model for the resonance frequency may be due to proximity effect.

Beyond thermal dependence, we have characterized the TLS contribution as a function of the driving power at 15 mK, where the condition $hf < 2k_B T$ is met and the thermal desaturation results in a power dependent resonator loss rate. As an example, Figure 4a shows the transmission spectra of a single Nb LER for different powers ranging from -120 dBm to -40 dBm. From

these values, the average number of photons in the resonator can be estimated using:

$$\langle n \rangle = \frac{Q_i^2 P_d}{Q_c h f_r^2} \quad (6)$$

Figure 4b shows Δf_r as a function of the number of photons for one LER from each chip at 15 mK. For the Nb resonator, we measured a positive resonance shift as $\langle n \rangle$ increases, which can be attributed to the gradual saturation of the resonant TLSs. Since the density of TLSs in the Nb/Au bilayer is not high enough to influence Δf_r , this upshift is not observed for this material. At even higher values of $\langle n \rangle$, the nonlinearity of the kinetic inductance dominates the physics of the system when the current density (J) in the resonator reaches a value J^* which sets the scale of the nonlinearity in the superconductor and it is close to the critical current density of the superconducting material [45]. As consequence, both LERs develop a strong asymmetric resonance response, which translates into a sharp jump in the transmission spectra and a negative relative frequency shift (see Figure 4a as an example). This nonlinear regime starts at $J^* = 3.58 \cdot 10^8 \text{ A} \cdot \text{cm}^{-2}$ for Nb and $J^* = 1.89 \cdot 10^8 \text{ A} \cdot \text{cm}^{-2}$ for Nb/Au, as expected from the higher kinetic inductance of the bilayer.

On the other hand, the inverse of the internal quality factor as a function of $\langle n \rangle$ at 15 mK is shown in Figure 4c. We observe an increase in Q_i for both devices above a certain critical value of the number of photons (n_c), which depends on the material. This enhancement originates in the competition between the driving power and the relaxation (γ_1) and decoherence rates (γ_2) of the resonant TLSs. The critical value is reached when the amplitude of the driving signal (i.e, the Rabi frequency $\Omega_R \sim \langle n \rangle^{1/2}$) increases beyond the system loss rate $\sqrt{\gamma_1 \cdot \gamma_2}$, since more of them are being locked onto their excited state [46]. Hence, resonant TLSs can absorb gradually less energy from the resonator and their contribution to the internal quality factor decreases.

In Figure 4c we also show with dashed lines the fit made upon the experimental data using the following expression [15], which relates the internal quality factor with the number of photons in the resonator:

$$\frac{1}{Q_i} = \tan \delta = F \cdot \tan \delta_{TLS}^0 \frac{\tanh \left(\frac{\hbar \omega_0}{2k_B T} \right)}{\left(1 + \frac{\langle n \rangle}{n_c} \right)^\beta} + \frac{1}{Q_i^{sat}} \quad (7)$$

Where $F \cdot \tan \delta_{TLS}^0$ is the loss tangent associated to the resonant TLSs in the low temperature and photon limits, β is a variable determined by TLS population densities and $1/Q_i^{sat}$ is the high-power loss, at which the resonant TLSs are saturated and other loss mechanisms start to dominate [17].

The slope in Q_i^{-1} is higher for Nb than for Nb/Au, a difference consistent with the larger TLS density in the former. From the fit to Equation (7), we extract $F \cdot \tan \delta_{TLS}^0 = 2.02 \cdot 10^{-6}$ for Nb, in agreement with the value reported by previous works [14], while for Nb/Au it is $F \cdot \tan \delta_{TLS}^0 = 9.68 \cdot 10^{-7}$. Furthermore, the critical number of photons is $n_c(Nb) = 6.93 \cdot 10^7$ photons and $n_c(Nb/Au) = 2.58 \cdot 10^6$ photons, whereas $\beta(Nb) = 0.12$ and $\beta(Nb/Au) = 0.05$, showing again the lower TLS density in Nb/Au in relation to Nb. Even at low driving power conditions, which is the optimal operation point for resonators in quantum computing applications and where the TLSs contribution is dominant, the Nb/Au device shows an internal quality factor higher than $Q_i \sim 10^6$, twice the value obtained for the Nb device.

Conclusions

In summary, we have fabricated superconducting lumped element resonators made of an Nb/Au bilayer and characterized their properties (resonance frequency and internal quality factor) as a function of temperature and driving power. We have compared our results by performing the same experiments in a nominally identical control sample fabricated of bare Nb. The microwave characterization in our Nb/Au and Nb devices matches our simulated designs in a consistent manner, proving a reliable manufacturing process. Adding the Au layer avoids Nb oxidation and reduces TLS loss while increasing the kinetic inductance of the device. Furthermore, we obtain internal quality factors higher than 1M for the Nb/Au devices even when the TLSs are not saturated, proving that the Au capping layer does not spoil the resonator properties but actually improves them. Overall, our results show that Nb/Au superconducting LERs outperform bare Nb ones with reference to the internal quality factor, TLS contribution, and responsivity. These properties are crucial for their application and integration into quantum electrodynamic circuits and radiation detectors. In particular, these devices allows an optimized integration of molecular spin-based quantum devices thanks to the ease of functionalizing the Au layer. The pristine metallic surface and its uniformity offer new possibilities in STM experiments. These findings impact the applicability of the resonators; the greater responsivity of the Nb/Au makes this material appealing for its implementation in single photon detectors for astronomical applications. In addition, the higher kinetic inductance and profound influence of nonlinearity in the Nb/Au physics make them more suitable to be applied as kinetic inductance parametric amplifiers.

Acknowledgments

This work has received support from grants TED2021-131447B-C22, PID2022-137779OB-C41 and PID2022-137779OB-C42, and HORIZON-MSCA-2021 Grant HyQuArch-101064707. The authors also acknowledge the research network RED2022-134839-T funded by the Spanish MCIN/AEI/10.13039/501100011033, by the EU “NextGenerationEU”/PRTR and by the “ERDF A way of making Europe”.

IMDEA Nanoscience acknowledges financial support from the ‘Severo Ochoa’ Programme for Centres of Excellence in R&D (CEX2020-001039-S) and CAB from the the CSIC Research Platform PTI-001 and from “Tecnologías avanzadas para la exploración del Universo y sus componentes” (PR47/21 TAU-CM) project funded by Com. de Madrid, by “NextGenerationEU”/PRTR.

Data Availability Statement

AIP Publishing believes that all datasets underlying the conclusions of the paper should be available to readers. Authors are encouraged to deposit their datasets in publicly available repositories or present them in the main manuscript. All research articles must include a data availability statement stating where the data can be found. In this section, authors should add the respective statement from the chart below based on the availability of data in their paper.

References

1. Blais, A., Huang, R.-S., Wallraff, A., Girvin, S. M. & Schoelkopf, R. J. Cavity quantum electrodynamics for superconducting electrical circuits: An architecture for quantum computation. *Phys. Rev. A* **69**, 062320 (6 June 2004).
2. Rosario, P., Santos, A. C., Villas-Boas, C. & Bachelard, R. Collateral Coupling between Superconducting Resonators: Fast High-Fidelity Generation of Qudit-Qudit Entanglement. *Phys. Rev. Appl.* **20**, 034036 (3 Sept. 2023).
3. Weichselbaumer, S. *et al.* Quantitative modeling of superconducting planar resonators for electron spin resonance. *Physical Review Applied* **12**, 024021 (2019).
4. Baselmans, J. *et al.* Ultra-sensitive THz microwave kinetic inductance detectors for future space telescopes. *Astronomy & Astrophysics* **665**, A17 (2022).
5. Padamsee, H. S. Superconducting radio-frequency cavities. *Annual review of nuclear and particle science* **64**, 175–196 (2014).
6. Gurevich, A. V. Tuning microwave losses in superconducting resonators. *Superconductor Science and Technology* (2023).
7. Krasnok, A. *et al.* Advancements in Superconducting Microwave Cavities and Qubits for Quantum Information Systems. *arXiv preprint arXiv:2304.09345* (2023).
8. Pappas, D. P., Vissers, M. R., Wisbey, D. S., Kline, J. S. & Gao, J. Two level system loss in superconducting microwave resonators. *IEEE Transactions on Applied Superconductivity* **21**, 871–874 (2011).
9. Martinis, J. M. *et al.* Decoherence in Josephson qubits from dielectric loss. *Physical review letters* **95**, 210503 (2005).
10. Béjanin, J. *et al.* Fluctuation spectroscopy of two-level systems in superconducting resonators. *Physical Review Applied* **18**, 034009 (2022).
11. Barends, R. *et al.* Reduced frequency noise in superconducting resonators. *Applied Physics Letters* **97**, 033507 (July 2010).
12. Barends, R. *et al.* Noise in NbTiN, Al, and Ta Superconducting Resonators on Silicon and Sapphire Substrates. *IEEE Transactions on Applied Superconductivity* **19**, 936–939 (2009).
13. Bruno, A. *et al.* Reducing intrinsic loss in superconducting resonators by surface treatment and deep etching of silicon substrates. *Applied Physics Letters* **106**, 182601 (May 2015).
14. Gao, J. *et al.* Experimental evidence for a surface distribution of two-level systems in superconducting lithographed microwave resonators. *Applied Physics Letters* **92**, 152505 (Apr. 2008).
15. McRae, C. R. H. *et al.* Dielectric loss extraction for superconducting microwave resonators. *Applied Physics Letters* **116** (2020).
16. Barends, R. *et al.* Minimal resonator loss for circuit quantum electrodynamics. *Applied Physics Letters* **97**, 023508 (July 2010).
17. McRae, C. R. H. *et al.* Materials loss measurements using superconducting microwave resonators. *Review of Scientific Instruments* **91** (2020).
18. Baselmans, J. Kinetic inductance detectors. *Journal of Low Temperature Physics* **167**, 292–304 (2012).

19. Rollano, V. *et al.* High cooperativity coupling to nuclear spins on a circuit quantum electrodynamics architecture. *Communications Physics* **5**, 246 (2022).
20. Chiesa, A. *et al.* Blueprint for a Molecular-Spin Quantum Processor. *Physical Review Applied* **19**, 064060 (2023).
21. Tabuchi, Y. *et al.* Hybridizing ferromagnetic magnons and microwave photons in the quantum limit. *Physical review letters* **113**, 083603 (2014).
22. Pirro, P., Vasyuchka, V. I., Serga, A. A. & Hillebrands, B. Advances in coherent magnonics. *Nature Reviews Materials* **6**, 1114–1135 (2021).
23. Verjauw, J. *et al.* Investigation of microwave loss induced by oxide regrowth in high-Q niobium resonators. *Physical Review Applied* **16**, 014018 (2021).
24. Guéron, S., Pothier, H., Birge, N. O., Esteve, D. & Devoret, M. Superconducting proximity effect probed on a mesoscopic length scale. *Physical review letters* **77**, 3025 (1996).
25. Hu, J. *et al.* Proximity-coupled Al/Au bilayer kinetic inductance detectors. *Journal of Low Temperature Physics* **199**, 355–361 (2020).
26. Valenti, F. *et al.* Interplay between kinetic inductance, nonlinearity, and quasiparticle dynamics in granular aluminum microwave kinetic inductance detectors. *Physical review applied* **11**, 054087 (2019).
27. Vissers, M. R. *et al.* Frequency-tunable superconducting resonators via nonlinear kinetic inductance. *Applied Physics Letters* **107** (2015).
28. Chien, W.-C. *et al.* Large parametric amplification in kinetic inductance dominant resonators based on 3 nm-thick epitaxial superconductors. *Materials for Quantum Technology* **3**, 025005 (2023).
29. Samkharadze, N. *et al.* High-kinetic-inductance superconducting nanowire resonators for circuit QED in a magnetic field. *Physical Review Applied* **5**, 044004 (2016).
30. Cornia, A., Mannini, M., Sainctavit, P. & Sessoli, R. Chemical strategies and characterization tools for the organization of single molecule magnets on surfaces. *Chemical Society Reviews* **40**, 3076–3091 (2011).
31. Gabarró-Riera, G., Aromí, G. & Sañudo, E. C. Magnetic molecules on surfaces: SMMs and beyond. *Coordination Chemistry Reviews* **475**, 214858 (2023).
32. Berti, G. *et al.* Scanning tunneling microscopy and spectroscopy characterization of Nb films for quantum applications. *Applied Physics Letters* **122** (2023).
33. Wang, Y. *et al.* Universal quantum control of an atomic spin qubit on a surface. *npj Quantum Information* **9**, 48 (2023).
34. Ghirri, A. *et al.* Self-assembled monolayer of Cr7Ni molecular nanomagnets by sublimation. *ACS nano* **5**, 7090–7099 (2011).
35. Vaxevani, K. *et al.* Extending the spin excitation lifetime of a magnetic molecule on a proximitized superconductor. *Nano Letters* **22**, 6075–6082 (2022).
36. *Sonnet User's Guide, Release 18* <https://www.sonnetsoftware.com/support>.
37. Probst, S., Song, F., Bushev, P. A., Ustinov, A. V. & Weides, M. Efficient and robust analysis of complex scattering data under noise in microwave resonators. *Review of Scientific Instruments* **86** (2015).
38. Day, P. K., LeDuc, H. G., Mazin, B. A., Vayonakis, A. & Zmuidzinas, J. A broadband superconducting detector suitable for use in large arrays. *Nature* **425**, 817–821 (2003).
39. Mattis, D. C. & Bardeen, J. Theory of the anomalous skin effect in normal and superconducting metals. *Physical Review* **111**, 412 (1958).
40. Zmuidzinas, J. Superconducting microresonators: Physics and applications. *Annu. Rev. Condens. Matter Phys.* **3**, 169–214 (2012).
41. Faoro, L. & Ioffe, L. B. Internal loss of superconducting resonators induced by interacting two-level systems. *Physical review letters* **109**, 157005 (2012).
42. Zhang, W. *et al.* Microresonators fabricated from high-kinetic-inductance aluminum films. *Physical Review Applied* **11**, 011003 (2019).
43. Zhao, S., Goldie, D. J., Withington, S. & Thomas, C. N. Exploring the performance of thin-film superconducting multilayers as kinetic inductance detectors for low-frequency detection. *Superconductor Science and Technology* **31**, 015007 (2017).
44. Barends, R. *et al.* Frequency and quality factor of NbTiN/Au bilayer superconducting resonators. **1185**, 152–155 (2009).
45. Swenson, L. *et al.* Operation of a titanium nitride superconducting microresonator detector in the nonlinear regime. *Journal of Applied Physics* **113** (2013).
46. Andersson, G. *et al.* Acoustic spectral hole-burning in a two-level system ensemble. *npj Quantum Information* **7**, 15 (2021).